



# Predicting Slope Instabilities in Salvador, Brazil, using Machine Learning and Georeferenced Data

Sandro Lemos Machado<sup>1</sup>, Guilherme Barbosa de Santana<sup>1</sup>, Miriam de Fátima Carvalho<sup>1</sup>, Jailma Santos de Souza de Oliveira<sup>1</sup>, Mehran Karimpour-Fard<sup>2</sup>, and Elio Perrone<sup>3</sup>

<sup>1</sup>Department of Materials Science and Technology, Federal University of Bahia, 02, Prof. Aristides Novis, Salvador, Postcode 40210-630, Bahia, Brazil

<sup>2</sup>School of Civil Engineering, Iran University of Science and Technology, Tehran, PO Box 16846-13114, Narmak, Iran

<sup>3</sup>Salvador City Hall, CODESAL, Salvador, 40285-600, Bahia, Brazil

**Correspondence:** Sandro Lemos Machado (smachado@ufba.br)

**Abstract.** Municipalities worldwide struggle with slope instability, a particularly pressing issue in cities such as Salvador, Brazil, where rugged terrain, escarpments, and complex geology create a high risk of instability. The complexity of the problem is evident in the variability of terrain properties, the bedrock's inherited structural features, and anthropogenic action. This range of variables makes it well-suited to machine learning (ML) approaches for instability prediction. Although ML has experienced an impressive recent boost, only a few cases have applied ML to real-world instability events. In this paper, a data bank of hydromechanical properties of soils is used in conjunction with a digital terrain model (DTM) and different georeferenced information, including rainfall, vegetation coverage, geological structures, sewage collection/treatment status, and residential density, to predict the occurrence of soil mass movements and related emergency calls to the municipality from the population living in risk areas. 13,522 emergency calls were considered during the period from 2020 to 2025. Excellent predictive performance, with an  $R^2 \approx 0.98$  consistently across both the validation and testing phases, was obtained in this original study. This strong result underscores the viability of machine learning as a powerful tool for this kind of problem, particularly within municipal warning systems.

**keywords** slope stability; risk assessment; geo-referenced data; machine learning; instability forecasting

## 1 Introduction

Slope stability analysis is a key branch of geotechnical engineering, a necessary tool for hazard prediction (Silva et al., 2008; Kinde et al., 2024). It is essential, along with other related knowledge areas such as debris flow (Fannin et al., 2015), to mitigate landslide risks that cause billions of dollars in economic damage annually and threaten lives and infrastructure. Traditional limit equilibrium methods (LEMs), such as Bishop's Simplified Method (Bishop, 1955) and Morgenstern-Price (Morgenstern and Price, 1965), and numerical techniques such as the Finite Element Method (FEM) and Strength Reduction Method (SRM), rely on assumptions about slip surfaces, soil homogeneity, and force equilibrium that struggle with uncertainties in soil properties (cohesion  $c$ ), friction angle ( $\phi$ ), unit weight  $\gamma$ ), geometry (height  $H$ ), angle ( $\beta$ ), pore pressure ( $r_u$ ), and external factors (seismicity, anthropic actions).  $c$ ,  $\phi$ , and  $r_u$  exhibit significant spatial-time variations (Trinidad and Momayez, 2025; Baecher,



2023), making it challenging to choose typical values for analysis, although they are related to the soil formations of the site and cannot be considered purely random. Several works recognize the importance of spatial correlation of geological properties (Griffiths and Fenton, 2004; Griffiths et al., 2009; Fenton and Griffiths, 2008; Ghasemian et al., 2024). Furthermore, data scattering is linked to the volume of soil mobilized in a test and the smaller the specimen, the greater the variability (Baecher, 2023). Probabilistic methods such as Monte Carlo simulation (Wang and Akeju, 2016; Mehdizadeh et al., 2020; Javankhoshdel and Bathurst, 2014) and the first order second moment (FOSM) (Wong, 1985; Phoon and Kulhawy, 1999) aim to mitigate some of these deficiencies, representing the variability and uncertainty inherent to natural geological structures, despite facing challenges in modeling the complex non-linear interactions that are inherent of the soil/rock masses (Trinidad and Momayez, 2025). Furthermore, the interactions between soil and environment, anthropic factors, and the scale of the simulation have a significant impact on the probability of slope instability events (Neves et al., 2025).

Data-driven based methods, including machine learning (ML), deep learning (DL), and soft computing techniques can leverage simulations, field data, and literature to model slope stability. By predicting the Factor of Safety ( $FoS$ ) or classifying stability status (e.g., stable, unstable), these approaches offer a powerful, data-centric solution for municipal decision-making in risk-prone areas, particularly when handling large, complex databases. Although many of the published papers deal with ML for  $FoS$  prediction (Ahangari Nanekharan et al., 2022; Yadav et al., 2025), ML techniques have proven applicable in a wide range of geotechnical problems, including landslide susceptibility mapping (Trinidad and Momayez, 2025), illustrating the versatility of ML and identifying opportunities for transference of cross-disciplinary knowledge and enhancement of slope stability analysis in large areas. In this regard, the ML models Random Forest and XGBoost are particularly valuable as they combine multiple learners, reducing overfitting while enhancing generalization in cases with substantial data uncertainty (Trinidad and Momayez, 2025).

This paper predicts landslide hazards in Salvador, Bahia, Brazil, using machine learning (ML) on georeferenced data. The model is trained using a novel data source: emergency calls from residents in areas at risk in Salvador, Bahia, Brazil, one of the few cities in Brazil with a consistent and reliable data set in this regard. Results of shear strength and permeability tests conducted by the geotechnical laboratories of the Federal University of Bahia over the past few decades are also used, along with the digital terrain model of the city (DTM), to calculate  $FoS$ , the probability of failure, and the reliability index in the entire urban area. The cumulative rainfall over periods ranging from 1 to 30 days prior to each event was estimated using data from 40 weather stations. This was used in conjunction with the mapped geological structures, including faults, foliations, and dikes, as variables influencing slope stability. As anthropic input layers, the presence of residences at both the top and the foot of the slope, as well as the quality of the sewage service around the slope, were evaluated. The developed framework can be helpful for municipalities in risk management activities and can provide a tool for online risk monitoring using rain data from city weather stations. Furthermore, the nature of ML enables frequent updates to the system, changing the DTM, residence, and sewage layers over time, and adding new emergency calls and rainfall data to the machine learning database.



## 55 2 Materials and methods

### 2.1 Soil formations and geological structural aspects

The urban area of the city of Salvador is formed of three geological-geomorphological domains: (i) the Recôncavo Sedimentary Basin; (ii) the Atlantic Coastal Margin; and (iii) the high Salvador. The Recôncavo sedimentary basin, formed from the evolution of the crustal stretching, which caused the fragmentation of the Gondwana supercontinent in the Mesozoic era (de  
60 Lima, 1999), is separated from the high Salvador by the main fault (fault 1,1 in Figure 1) of the region (locally known as the high city and the low city). The high city, where most of the landslides occur has a complex geological history, with different kinds of metamorphic rocks with high degrees of metamorphism, often cut by diabase and granitic dikes (Barbosa et al., 2005; Souza and Gandolfo, 2012). The metamorphic rocks are essentially 1) orthoderived metamorphic rocks of quartz-feldspathic composition, light to dark gray in color (Souza-Oliveira et al., 2014); ii) paraderived metamorphic rocks (Souza and Gandolfo,  
65 2012) of dark gray color; and iii) mafic (metagabbros) and ultramafic (metapyroxenites) enclaves, commonly associated with paraderived granulites in the form of boudins (Souza-Oliveira et al., 2014).

With the separation of the Gondwana supercontinent and the formation of the south Atlantic in the Mesozoic, a brittle phase developed, correlated with the opening of the Brazilian marginal basins, among them the Recôncavo Sedimentary Basin, forming faults and fractures, which can be grouped according to their orientation into:

- 70 1. N020°-N030° - faults *cidade alta-cidade baixa* (high-low city, 1,1 in Figure 1), Iguatemi (1,2) and *Jardim de Alah* (1,3) and their reverberations.
2. N120°-N130° and N130°-N140° faults parallel to the system *Mata-Catú* (2) (Barbosa et al., 2005; Nascimento, 2008).
3. N080°-N090° fault of *Barra* (3).

### 2.2 Databank

75 The Databank used in the research comprises 350 results of drained triaxial (ASTM-D7181, 2011) and direct shear (ASTM\_D3080, 2012) tests performed on saturated and natural water content undisturbed samples collected in the city of Salvador from 2005 to 2022 by Geotechnical (mainly) and Geoenvironmental laboratories of the Federal University of Bahia. Only data providing a satisfactory location (geocoordinates, street address, or a well-known building) were considered. As observed in Table 1 and Figure 1, most of the data (232 samples) come from the crystalline bedrock's residual soil of Granulite/Gnaiss, which  
80 is coherent with the dominant presence of this soil in the urban area. The second most frequently tested formation (68 samples) is the Barreiras sedimentary formation, which typically occupies elevations above 70 m in the city (Figure 1). These two formations encompass almost the entirety of the slopes analyzed due to their predominance in the superficial soil, particularly in slope areas. The samples of residual of Granulite/Gnaiss presented the highest plasticity and clay & silt content. Apart from the residual soil and Barreiras formations, the Quaternary formations are discontinuous, and the geological map scale can

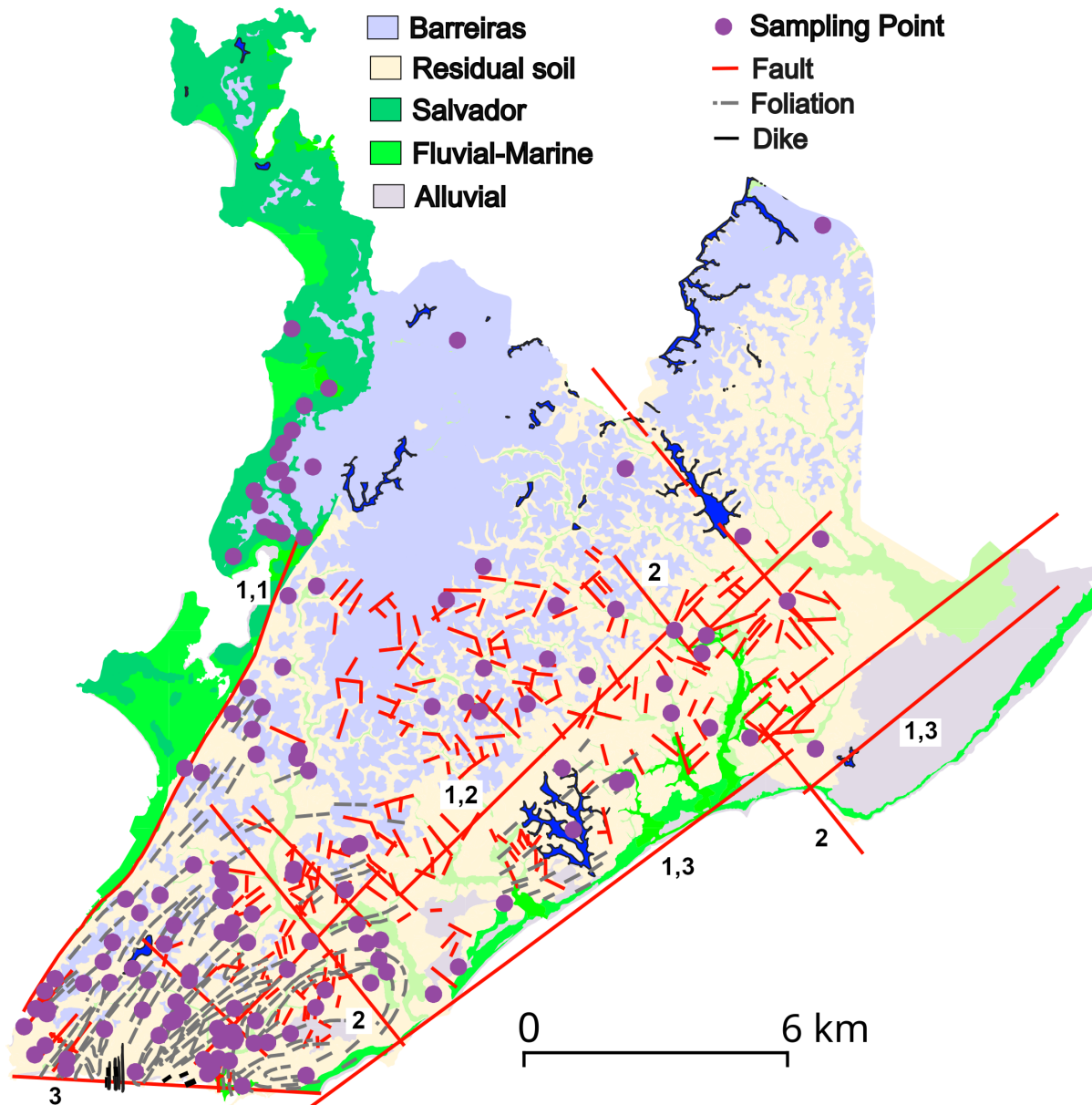


**Figure 1.** Presence of the main soil formations at surface, sampling points and geological aspects

85 influence the genesis attributed to the samples. Due to the high scattering, the values of  $k$  presented in Table 1 express only the order of magnitude of the expected value of permeability for the soil.

Reflecting the observed variability in terms of Atterberg limits, soil formations also presented high variability in terms of shear strength parameters (Table 2), mainly for tests performed in *natural water content*, and for cohesion intercept, since no



**Table 1.** Databank distribution by formation and geotechnical typical results.

Formation	n	$W_L$ (%)	$W_P$ (%)	$PI$ (%)	$k$ (cm/s)	Sand & gravel (%)	Clay & silt (%)
Crystalline bedrock's residual soil	232	$58 \pm 12.7$	$36 \pm 6.3$	$21 \pm 8$	$5 \times 10^{-6}$	$34.2 \pm 12.9$	$68.3 \pm 9.6$
Barreiras sedimentary formation	68	$45 \pm 7.5$	$28 \pm 5.3$	$17 \pm 6.7$	$1 \times 10^{-4}$	$52.4 \pm 10.0$	$48 \pm 10.0$
Salvador formation	21	$46 \pm 12$	$28 \pm 5.3$	$18 \pm 8.7$	$1 \times 10^{-7}$	$48.4 \pm 17.1$	$49.6 \pm 15.9$
Quaternary alluvial sediment	14	$53 \pm 7.3$	$33 \pm 6.2$	$19 \pm 5.9$	$1 \times 10^{-4}$	$39.5 \pm 10.7$	$60.5 \pm 10.7$
Quaternary Fluvial-Marine	15	$50 \pm 4.1$	$32 \pm 7.2$	$18 \pm 6.3$	$1 \times 10^{-4}$	$33.3 \pm 13.1$	$66.7 \pm 13.1$

Obs: mean  $\pm$  std. dev. values.

water content control is applied in the tests (commercial demand of consultants to the laboratories) and the soil's moisture changes over the course of the year. All the formations exhibited high spatial variability, and the different specimen positions in the weathering profile also increased the variability of the residual soils. The idea of the research was to use a Databank that is continuously updated by consultants who require shear strength tests to be conducted at our facilities as part of their activities. Besides the expected values of shear strength parameters, all the observed variability was taken into account in the slope calculation, as discussed below. The correlation coefficient between friction angle ( $\phi$ ) and cohesion ( $c'$ ), ( $cor_{\phi-c}$ ) was always negative, as reported by many authors in literature (Lumb, 1970; Cherubini, 2000; Wang and Akeju, 2016), however, with different intensities, and was also considered in the performed slope stability calculus. In Table 2, the subscripts *nat* and *sat* stand for natural water content and saturated specimens, respectively, and  $\gamma$  is the unity weight of the soil.

**Table 2.** Shear strength parameters and variability of soil formations.

Formation		$\gamma_{nat}$ (kN/³)	$\phi_{nat}$ (°)	$c'_{nat}$ (kPa)	$cor_{\phi-c}$	$\gamma_{sat}$ (kN/³)	$\phi_{sat}$ (°)	$c'_{sat}$ (kPa)	$cor_{\phi-c}$
Crystalline bedrock's residual soil	Mean	15.7	31.3	50.1	-0.08	16.1	29.1	20.9	-0.29
	Std. Dev.	1.70	4.91	28.86					
Barreiras sedimentary formation	Mean	16.0	30.5	37.2	-0.20	16.3	30.5	12.4	-0.33
	Std. Dev.	2.23	5.63	27.93					
Salvador formation	Mean	16.3	32.4	37.9	-0.69	16.6	27.0	12.4	-0.38
	Std. Dev.	1.56	10.35	18.42					
Quaternary alluvial sediment	Mean	14.4	30.0	39.6	-0.07	13.8	30.4	11.1	-0.58
	Std. Dev.	1.88	7.15	19.05					
Quaternary Fluvial-Marine	Mean	16.3	32.8	76.0	-0.12	16.7	27.6	18.7	-0.44
	Std. Dev.	0.93	5.67	45.43					



## 2.3 The machine learning model

### 2.3.1 Input variables

#### 100 Slope stability results

A Python script was developed to isolate slope areas using the [digital terrain model of the city](#). The entire city’s DTM is of a size of approximately 4.5 GB (5,4299 × 5,3010 pixels) and a horizontal resolution of 0.5 m. Areas with a declivity higher than 18% were isolated, and the top of the slope was identified. Then streamlines were traced at 5-meter intervals along the top, and the slope sections were drawn by linking the beginning and end of each streamline (the slope’s crest and foot) with a straight line. Using this method, around 775,500 slopes were calculated for the entire city. [Figure 2a](#) shows a portion of the urban area where the slope areas were selected and the streamlines traced.

105

For  $FoS$  calculation, the slope stability charts by [Michalowski \(2002\)](#) ( $r_u = 0$ ) were digitized and fitted by [Equation 1](#)

$$\frac{FoS}{\tan(\phi)} = a + \frac{b x + c x^2}{1 + x} \quad (1)$$

where  $x = c' / [\gamma H \tan(\phi)]$ ,  $H$  is the slope height,  $FoS$  is the slope’s Factor of Safety and  $a$ ,  $b$  and  $c$  are fitting constants for each slope angle ( $\beta$ ) of the Michalowski’s charts. All the fitted curves presented values of  $R^2 > 0.999$ , and the equation’s performance was considered adequate. [Figure 2b](#) illustrates the slopes and the obtained values of  $FoS$  (saturated condition) for the areas illustrated [Figure 2a](#).

110

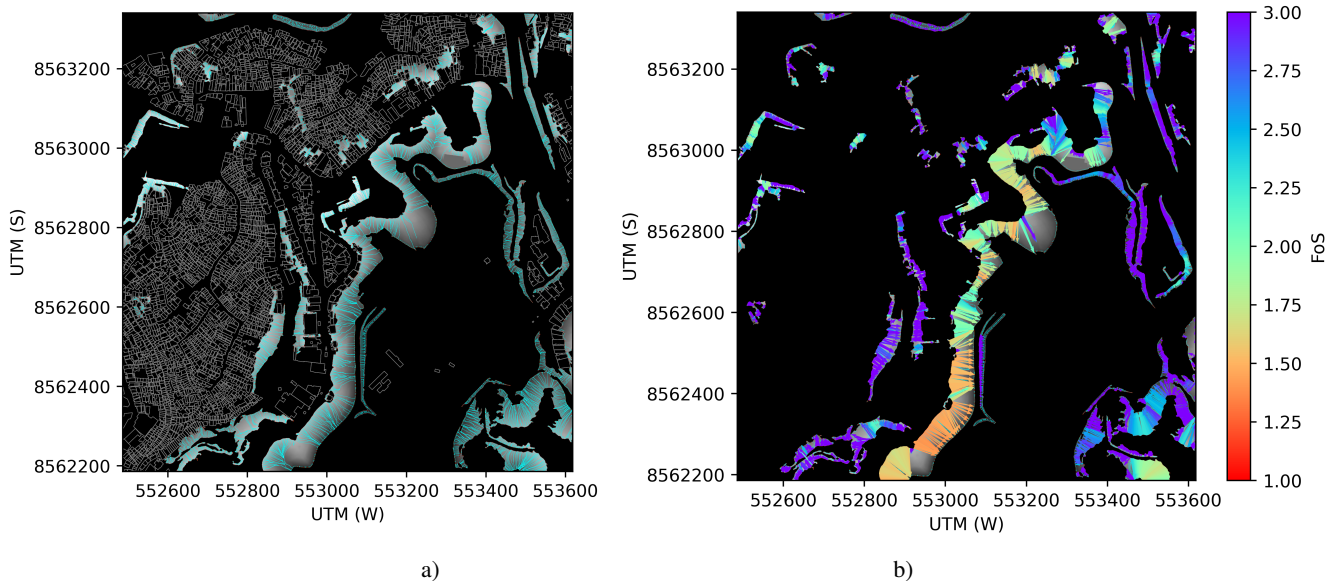


**Figure 2.** Example of slope areas calculation from DTM. a) resulting streamlines and b) calculated  $FoS$ .



The variability presented in Table 2 for  $\gamma$ ,  $c'$  and  $\phi$  for each condition (natural and saturated) were used with the concepts of the First Order Second Moment method (Wong, 1985) to calculate the  $FoS$ 's standard deviation (Std Dev,  $\mu$ ) and the probability of failure ( $PF$ ) of the slope (Equation 2). The FOSM method is a probabilistic technique for uncertainty and reliability analysis that uses a first-order Taylor series approximation of a function, along with the first and second moments (mean and variance) of the random input variables. This method simplifies reliability analysis by assuming the function can be linearized at the mean values of the inputs and that the output has a normal distribution. It is widely used due to its relative simplicity, however, it can be inaccurate if the function's behavior at the mean is significantly different from the actual value. Despite presenting spatial variability and dependence of the soil's genesis/classification, the unit weight and the shear strength parameters were assumed to be random within the same soil formation.

$$\mu_{FoS} = \sqrt{\sum_{i=1}^n \left[ \frac{\partial Fos}{\partial x} \right]_i^2 \mu_{x_i}^2 + \sum_{i=1}^n \sum_{j(j \neq i)=1}^n \frac{\partial Fos}{\partial x_i} \frac{\partial Fos}{\partial x_j} COV_{x_i x_j}} \quad (2)$$

where  $\mu_x$  is the Std Dev of the variable  $x$  (i.e.,  $\gamma$ ,  $c'$ , and  $\phi$ ) and  $COV_{x_i x_j}$  is the coefficient of variation between the variables  $x_i$  and  $x_j$  (only the covariance between  $c'$  and  $\phi$  was considered, using the  $cor_{\phi-c}$  values presented in Table 2). The  $\partial Fos / \partial x$  values were calculated using the finite difference concept ( $\partial y / \partial x \approx \Delta y / \Delta x$ ), varying the values of  $\gamma$ ,  $c'$ , and  $\phi$  by 1% and observing the corresponding variation in  $FoS$ .

Once the values of  $\mu_{FoS}$  were obtained, the probability of failure was calculated. This was the same as that for obtaining  $FoS < 1$  (normal distribution assumed) and the reliability index ( $\beta_r$ ) was calculated using

The  $FoS$  and  $\beta_r$  values obtained using the script were compared with those by Slide2<sup>®</sup> (RocScience, 2025), adopting the Morgenstern and Price (1965) method with a half sine interslice force function.  $\beta$  values ranged from 30° to 45° and values of  $H$  10 - 20 m were adopted, with values of  $c'$  of 5, 15, and 25 kPa and  $\phi$  of 30° and 35°. The semi-probabilistic analysis used the Monte Carlo method with a number of samples ( $N$ ) of 60,000 and the overall slope statistical analysis option, where the entire slip surface search is repeated  $N$  times. Some analyses were performed using  $N > 60,000$  with no noticeable change in the observed results. As illustrated in Figure 3, the mean difference in the  $FoS$  values between the two methods was  $\overline{FoS_{err}} = 0.0271$ , with a  $\mu Fos_{err} = 0.0498$ , whereas values of  $\overline{\beta_{r_{err}}} = -0.104$  and  $\mu \beta_{r_{err}} = 0.163$  were rendered, confirming the compatibility between the two methods of analysis.

Figure 4 illustrates some of the input layers and the emergency calls in the period of analysis used in the machine learning process. As observed, most of the emergency calls to the municipality are concentrated in areas with low  $FoS_{sat}$  values. 13,522 emergency calls were analyzed in this paper, including both confirmed and non-confirmed mass movements.

#### 140 Additional input layers

Besides the values of  $FoS_{sat}$ ,  $FoS_{nat}$ ,  $PF_{sat}$ ,  $PF_{nat}$ ,  $\beta_{rsat}$  and  $\beta_{rnat}$  calculated for each slope, additional information was used in the machine learning process. For most of the input layers, a radius of influence ( $R_i$ ) (see Figure 5) was drawn at the midpoint of each slope to define an area of influence ( $Ia$ ). Only the georeferenced information inside the  $Ia$  was considered in the performed analysis.

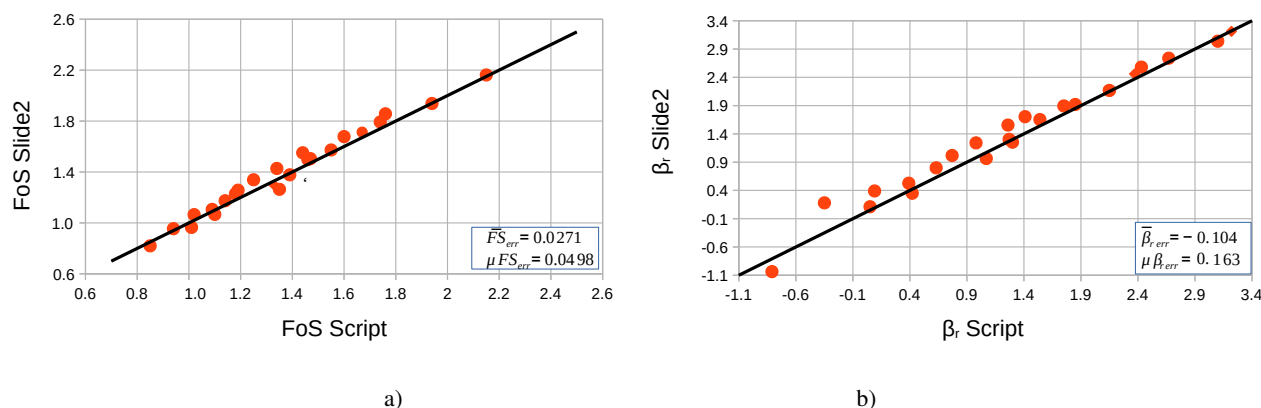


**Figure 3.** Comparison between developed Python script and Slide2<sup>®</sup> (RocScience, 2025) in terms of a)  $FoS$  and b)  $\beta_r$ .

145 This was the case with the geological aspects of the city. The script searches each eligible slope (slopes having at least one emergency call in the period of analysis inside  $Ia$ , as illustrated in Figure 5) for the geological structures shown in Figure 1 (faults, foliations, and dikes) and calculates the sine of the angle ( $\theta$ ) between the structure and the line defining the slope itself, generating an input value. Slopes with no structures inside  $Ia$  had a zero structure value. For slopes with more than one structure in the vicinity, the closest structure was considered. Faults, foliations, and dikes were considered separately. As  
150 illustrated in Figure 1, the area of the high city is formed superficially mainly of residual soils from crystalline rock weathering, which contain relic structures that may form preferential failure surfaces, conditioning slope stability (Stead and Wolter, 2015; Santana, 2021).

The presence of residences in the  $Ia$  (i.e., Figure 2a and Figure 5) was also considered using the residence layer provided by the local municipality. Two input variables were derived as the ratio between the occupied area and the  $Ia$  in the slope body  
155 and top, and in the neighboring of the slope's foot. This distinction is necessary because the residences located in the vicinity of the slope's foot tend to have a stabilizing effect, in contrast to those observed at the top of the slope and along its length. A further data layer provided by the municipality was the vegetation cover of the slope. In this case, the input variable for each eligible slope was the ratio between the vegetation area and the slope's  $Ia$ .

The weather stations presented in Figure 4 provided hourly information on rainfall in the period of analysis. For each  
160 eligible slope, the accumulated rainfall for 1d, 2d, 3d, 5d, 7d, 10d, 15d, and 30d was calculated using as reference the date of the emergency call and the values registered in the weather stations, which were interpolated using the inverse of the square distance as weight.

The Brazilian Institute of Geography and Statistics (IBGE) and the Institute for Applied Economic Research (IPEA) published recently data concerning the quality of the sewage services in Brazil, which is available for analysis using a R<sup>®</sup> (ter  
165 Braak and Šmilauer, 2018) package titled *CensoBr* (Pereira and Barbosa, 2023). For the city of Salvador, Bahia, information about the sewage system is provided for 4,541 census sectors (Figure 4). For each sector, the quality of the sewage service was evaluated as a weighted mean by the number of residences for the following conditions:

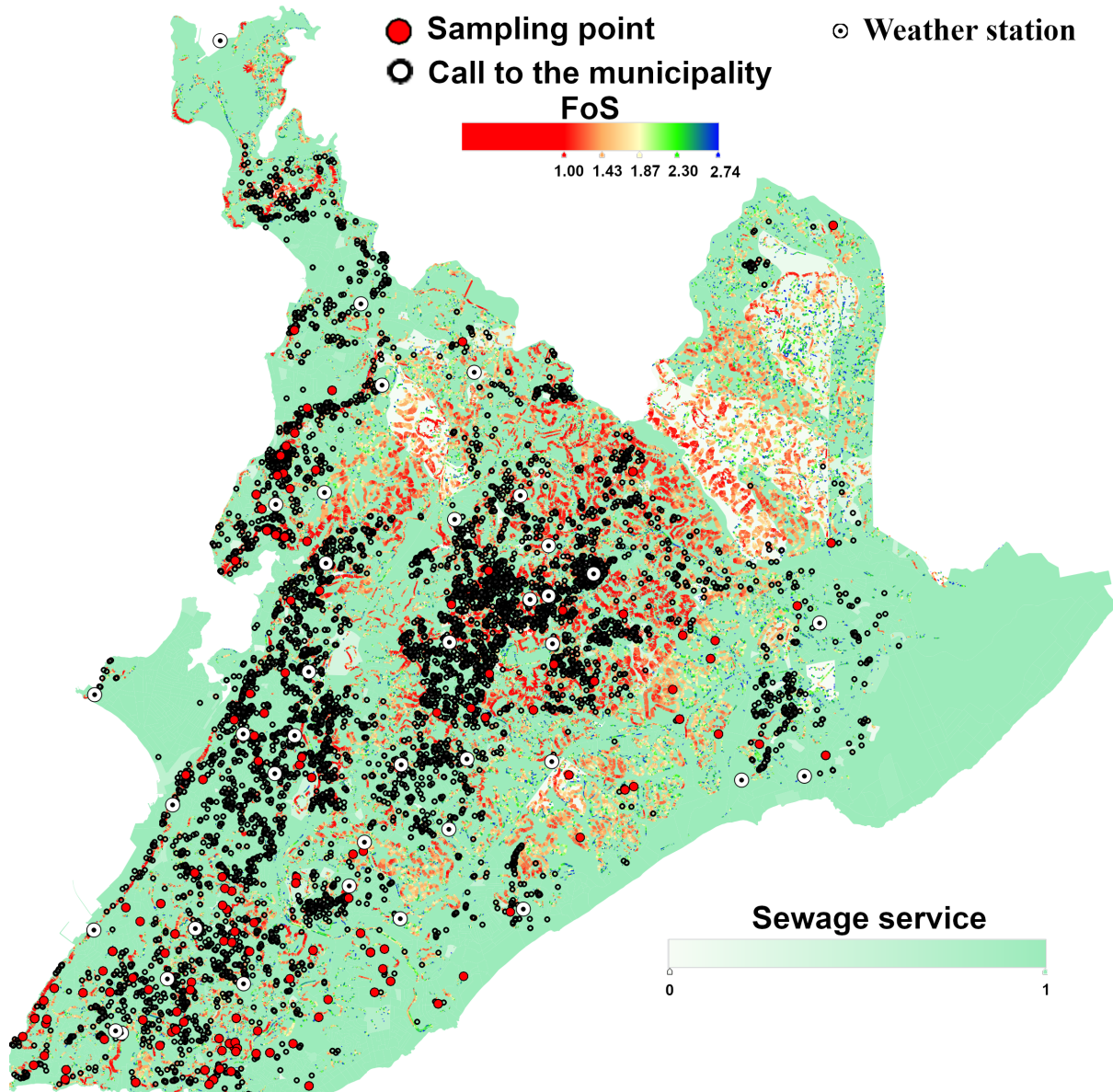


**Figure 4.** Map with some input layers and the emergency calls to the municipality used to calculate the output variable.

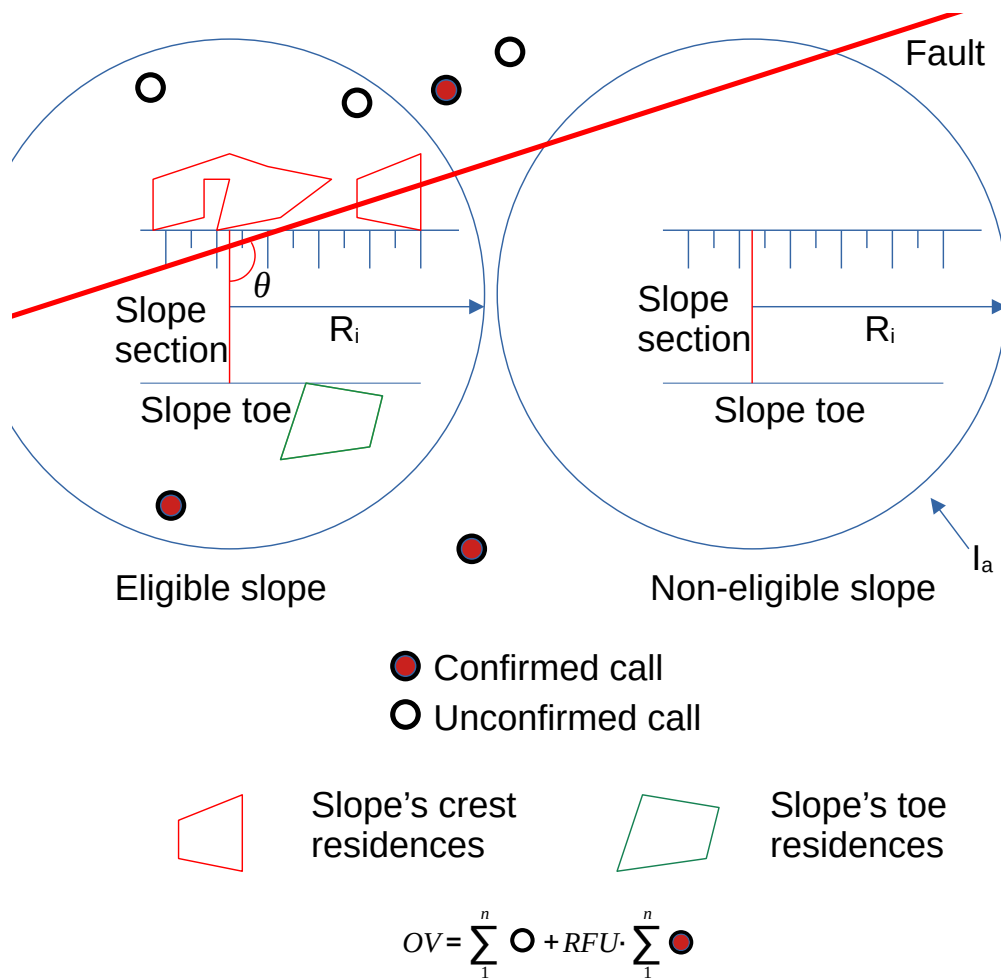


**Figure 5.** Illustration of the calculation process of input and output variables



- No sewage collection system and no septic tank or pit - 0
- Sewage disposal in a rudimentary pit - 0.1
- 170 – Sewage disposal in a non-engineered septic tank - 0.2
- Sewage disposal in an engineered isolated septic tank - 0.3
- Sewage disposal in an engineered septic tank linked to the sewage collection system - 0.6
- Sewage disposed in the sewage collection system - 1.0

This input variable reflects the development status of the population in the census sector and, to some extent, the presence  
175 of the public services. Furthermore, areas with no sewage collection systems (and probably no proper drainage systems) suffer  
from what may be called anthropic rainfall, as practically all the sewage water infiltrates the terrain along with part of the  
rainfall.

Finally, in some regions, a preliminary stabilization procedure composed of slope cover with nonwoven geotextile and  
shotcrete has been applied by the municipality, with potential positive impacts on the slope stability. Therefore, for each  
180 eligible slope, the script checks for the existence of stabilization measures prior to the emergence call date. Only two values  
are assigned to this variable: 0 or 1.

### 2.3.2 The output variable and considered scenarios

The output (*OV*) variable was calculated considering the number of confirmed and unconfirmed calls made to the municipality  
in the slope's radius of influence and within a time interval ( $T_i$ ), as illustrated at the bottom of [Figure 5](#).

185 Different scenarios performed by varying some analysis parameters were produced for machine learning training. The pa-  
rameters that were changed in the performed analysis were:

- Slope's radius of influence  $R_i$ . Adopted values of 75m, 100m, 150m, 200m, and 300m
- Time interval, in days, before the emergence call date, in which the calls are assumed as part of a unique event. Adopted  
values of 2-6d
- 190 – Ratio failure/unconfirmed call (RFU) weight. Adopted values of  $RFU$  of 5, 10, 20, and 30

During the rainy season, the emergency calls are seldom just received on one single day and may be received over periods  
longer than one week. Therefore, the machine learning procedures were repeated for different  $T_i$  values so as to maximize the  
 $R^2$  value in the validation and testing phases of the ML process. Furthermore, only some of the emergency calls were about  
a mass movement later confirmed in the field by the municipality staff. In order to take this into consideration in the analysis,  
195 confirmed calls were given a higher weight (RFU value) in the output variable value, which is calculated as the weighted sum  
of all the calls in the adopted  $T_i$ . Unconfirmed calls were attributed a unity value.



Increasing  $RFU$ ,  $T_i$ , and  $R_i$  also increases the value of the output variable. Analysis performed with a higher  $R_i$  will encompass a larger area with a higher potential number of emergency calls. The combinations of slopes and emergence calls for each radius of influence, for the period of analysis, yielded approximately 2,000,000 points for each  $RFU$ ,  $T_i$ , and  $R_i$ , which were modeled as described below.

### 2.3.3 Adopted machine learning procedure

The ML procedure used the `XGBRegressor`, a Gradient Boosting algorithm based on trees. The `XGBRegressor` is a class within the `XGBoost` library that implements gradient boosted decision trees for regression tasks. It is a powerful and popular machine learning algorithm known for its efficiency, flexibility, and performance (Chen and Guestrin, 2016).

Constructing an efficient ANN requires optimizing the various parameters of the model to reach an optimal network configuration. This optimized configuration enables the ML algorithm to establish complex predictive relationships, making ML a powerful and versatile tool in various scientific fields. The optimization process can use empirical (i.e., by trial and error) procedures, which gradually increase the ML model's complexity, or use optimization algorithms, such as Hyperband (Li et al., 2018; Dos Santos Pereira et al., 2025) or the `RandomizedSearchCV` (Pedregosa et al., 2011).

During the training phase, the `RandomizedSearchCV` by `scikit-learn` library automatically provided the optimized hyperparameters. This method is an alternative to `GridSearchCV`, and is especially useful when the hyperparameter search space is large. For each  $R_i$ ,  $T_i$ , and  $RFU$  combination, the hyperparameters  $n\_estimators$ ,  $learning\_rate$ ,  $max\_depth$ ,  $subsample$ ,  $colsample\_bytree$ ,  $reg\_alpha$ , and  $reg\_lambda$  were optimized seeking for the maximum  $R^2$  of the validation subset.

For each combination of  $RFU$ ,  $T_i$ , and  $R_i$ , the Databank was stratified based on the values of the output variable into 10 classes using 10 percentiles (from 10% to 90%), and then randomly split into subsets with 60% (training), 20% (validation), and 20% (testing) of the whole Databank. The test subset remained unseen by ML model during the entire training procedure.

## 3 Results and analysis

Figure 6 summarizes all the obtained results in the machine learning attempts performed. As observed, in all the scenarios, ML was able to deliver a very good and similar performance for the testing and validation Databanks, with values of  $R^2 > 0.94$ .

Table 3 summarizes the best results obtained for each  $R_i$  presented in Figure 6, and Figure 7 and Figure 8 illustrate how the slope's radius of influence and  $RFU$  impact the ML performance. As observed,  $R_i$  had the most significant impact on ML predictive ability, with the most substantial  $R^2$  values obtained for  $R_i = 300$  m. Furthermore, the influence of  $RFU$  and  $T_i$ , indicated by the dispersion bars, decreases with  $R_i$ . However, using such a large radius of influence may capture emergency calls from adjacent areas and relatively distant structural aspects of the bedrock, as illustrated in Figure 9, where circles with  $R_i$  of 150m and 300m were traced in a typical area of risk in the city.

Using a  $RFU=20$  led to slightly better results for all the  $R_i$ . Using a time interval of 4 days, in most cases, resulted in a better performance, although the  $T_i$  influence was considered negligible. Figure 6c presents the ML performance for a  $R_i=150$  m with varying  $T_i$  and  $RFU$ , chosen as the best option in terms of  $R_i$  considering the individuality of each slope area.

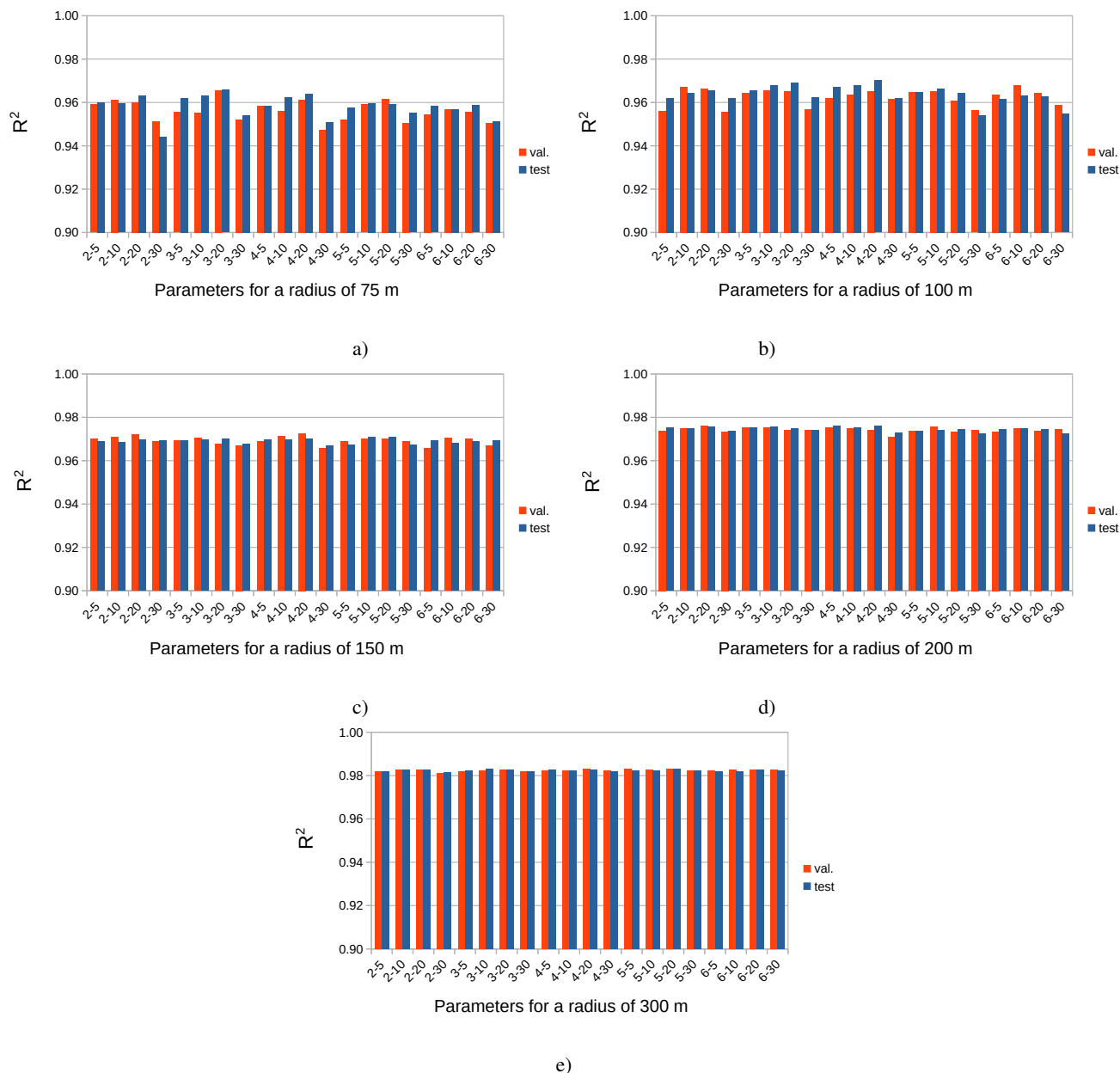


**Figure 6.** ML performance for a)  $R_i=75$ m; b)  $R_i=100$ m; c)  $R_i=150$ m; d)  $R_i=200$ m and w)  $R_i=300$ m, with varying  $T_i$  and  $RFU$ .

230 **Figure 10** shows the ML performance for a  $R_i=150$ m,  $T_i=4$ d and  $RFU=20$ . Although the presence of relatively few scattering points (about 360,000 experimental points are presented in the graph), the ML model presents a similar and excellent performance in both the validation and test phases. In `XGBoost`, "weight" and "gain" are key concepts related to feature importance and the tree building process. The weight refers to the number of times a feature is used to split the data across all



**Table 3.** Best machine learning performances for each radius.

$R_i$ (m)	$T_i$	$RFU$	Phase	MAE	MSE	RMSE	$R^2$
75	3	20	Val.	1.1743	18.4881	4.2998	0.9656
			Test	1.1589	17.9096	4.232	0.9658
100	4	20	Val.	1.1399	19.6267	4.4302	0.9654
			Test	1.1227	17.8757	4.228	0.9702
150	4	20	Val.	1.1103	17.7312	4.2108	0.9726
			Test	1.1274	19.2145	4.3834	0.9699
200	4	10	Val.	1.1264	18.7804	4.3336	0.9741
			Test	1.1138	18.1603	4.2615	0.976
300	4	20	Val.	1.1434	16.6599	4.0817	0.983
			Test	1.1409	16.9099	4.1122	0.9827

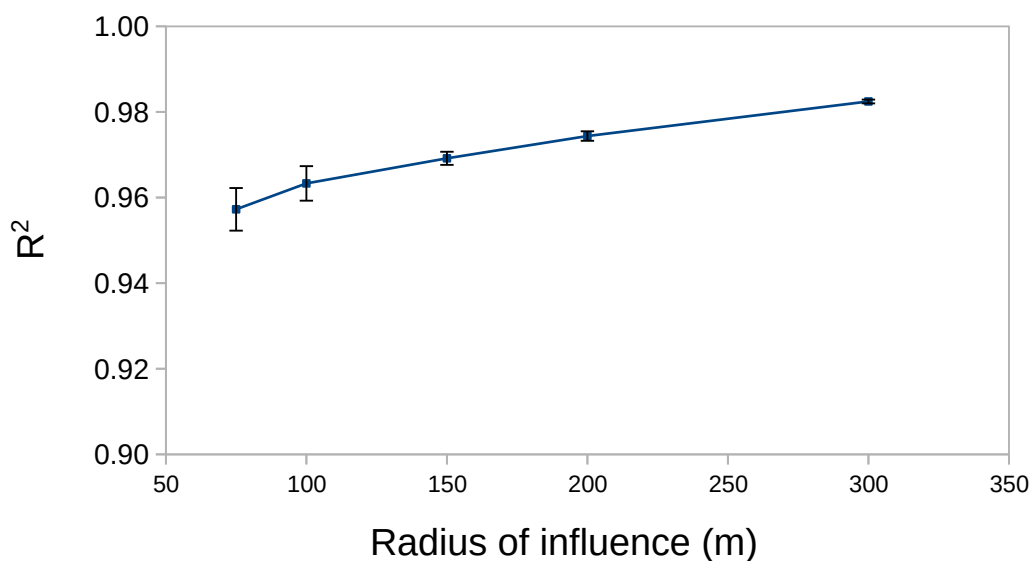


**Figure 7.** ML performance as a function of  $R_i$

trees in a given XGBoost model, whereas the gain is linked to the reduction in training loss achieved when using a feature for splitting. The gain quantifies the improvement in the model’s performance (reduction in the objective function) achieved by using a particular feature to make splits throughout the ensemble of trees. As observed in Figure 11a, the variables related to

235

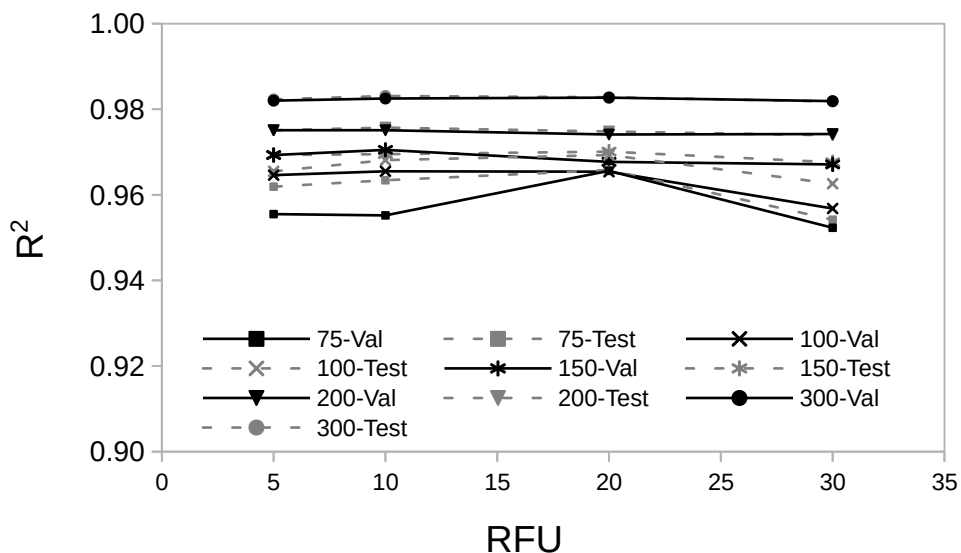


Figure 8. ML performance as a function of  $RFU$



Figure 9. Illustration of the  $R_i$  effect merging data from different adjacent slopes

the slope stability analysis, both in natural and saturated states (probability of failure and  $FoS$ ), and the different periods of cumulative rainfall, had the highest weight values. The quality of the sewage service also had a significant influence on the



obtained results, followed by vegetation cover, structural geological aspects, and the density of residences. Figure 12 compares the feature's weight for different values of  $R_i$ . Although the list of parameters with higher weights remains almost unchanged, the relative weight of the sewage service increases with  $R_i$ , going from 14<sup>th</sup> to 8<sup>th</sup> place when  $R_i$  increases from 75m to 300m. According to Figure 11, the input variables for different periods of rainfall presented high values of both weight and gain, meaning that they are often used in splitting data and are effective in improving the model performance. Vegetation cover, the presence of buildings, and faults in the bedrock tend to form a second platoon in terms of variable weight; however, permeability and faults in the bedrock contribute to the first platoon in terms of gain.

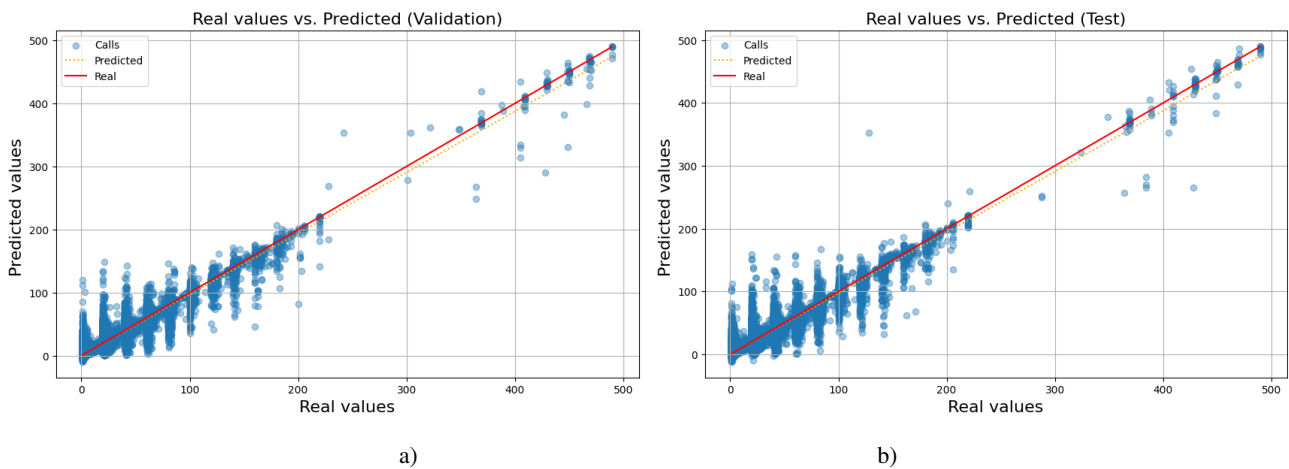


Figure 10. ML results for  $R_i=150m$ ,  $RFU=20$ , and  $T_i=4d$ . a) validation and b) test phases

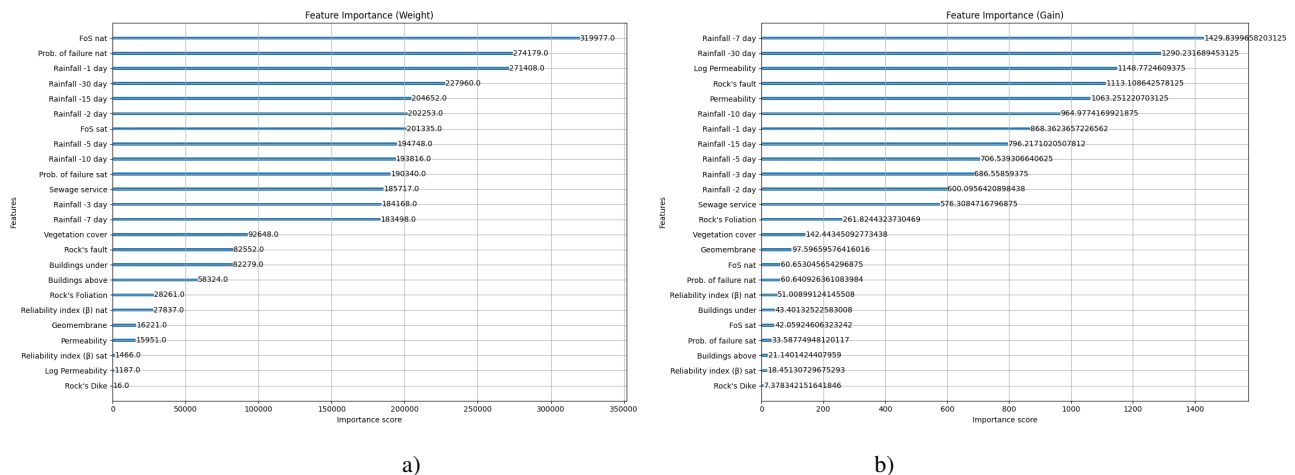


Figure 11. Importance of the features (input parameters) on the ML performance in terms of a) weight and b) gain ( $R_i=150m$ ,  $RFU=20$  and  $T_i=4d$ )

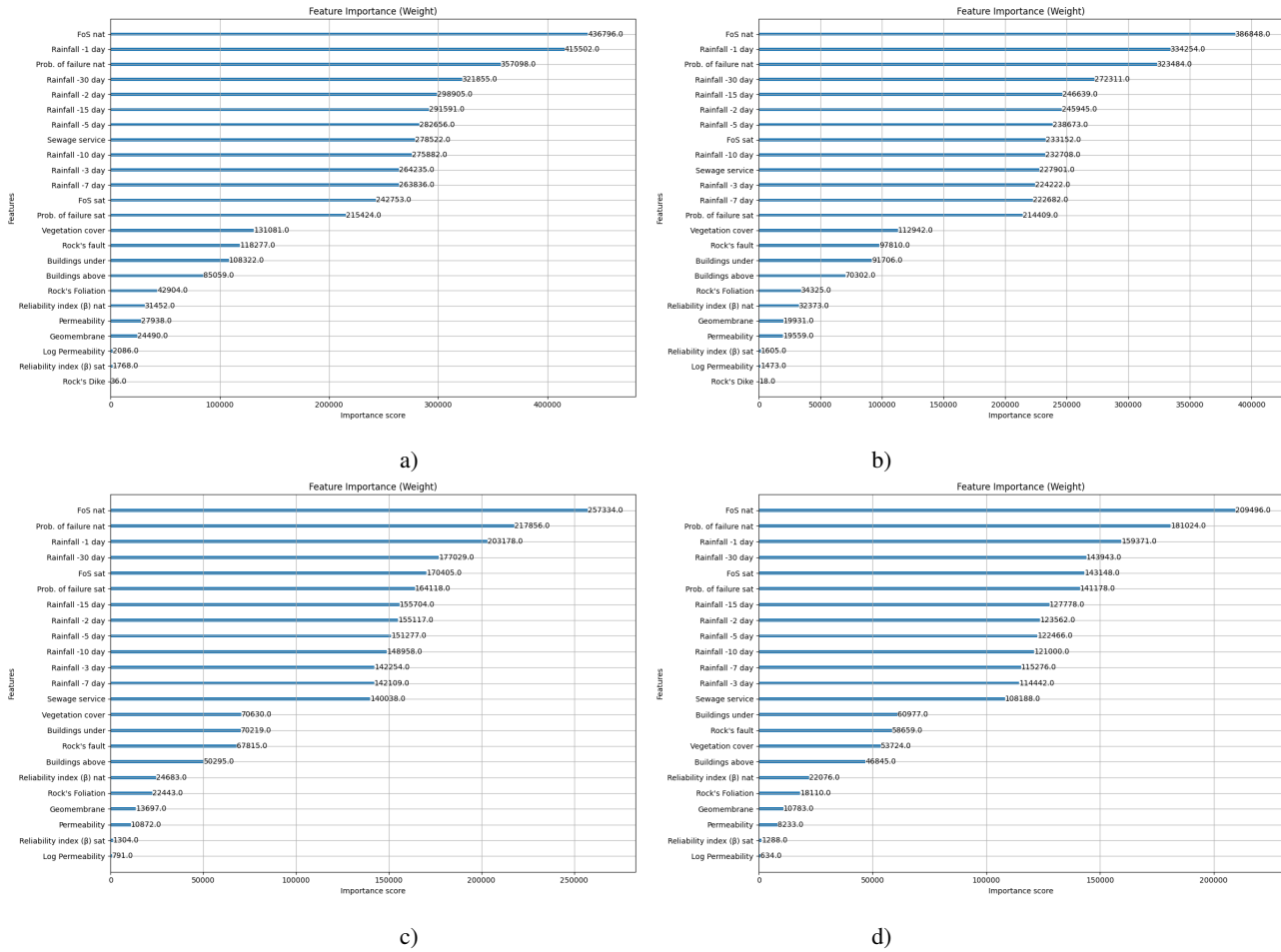


Figure 12. Importance of the features (input parameters) on the ML performance in terms of weight for different  $R_i$  values

245 Figure 13 compares the feature's gain for different values of  $R_i$ . The cumulative rainfall inputs still tend to present the highest gains. However, the soil permeability and the faults in the bedrock play a first-level role in this case. The faults in the bedrock lose gain as  $R_i$  increases, reaching the 2<sup>th</sup> place for  $R_i=75$ m and the fourth position for  $R_i=100$ m and  $R_i=150$ m. The same pattern is observed for the soil permeability, whereas the quality of the sewage service tends to preserve an intermediate ranking. These findings also suggest that using  $R_i = 150$  m is a wise choice because it tends to ensure greater effectiveness

250 for variables other than those linked to rainfall. In gradient boosting, variables that have the highest "weight" (the number of times used in a split) may present smaller "gains" (reductions in loss) in later trees because earlier trees have already captured the most significant predictive power of that feature. Gradient boosting is an iterative process where each new tree is built to correct the errors (residuals) of the previous ones.

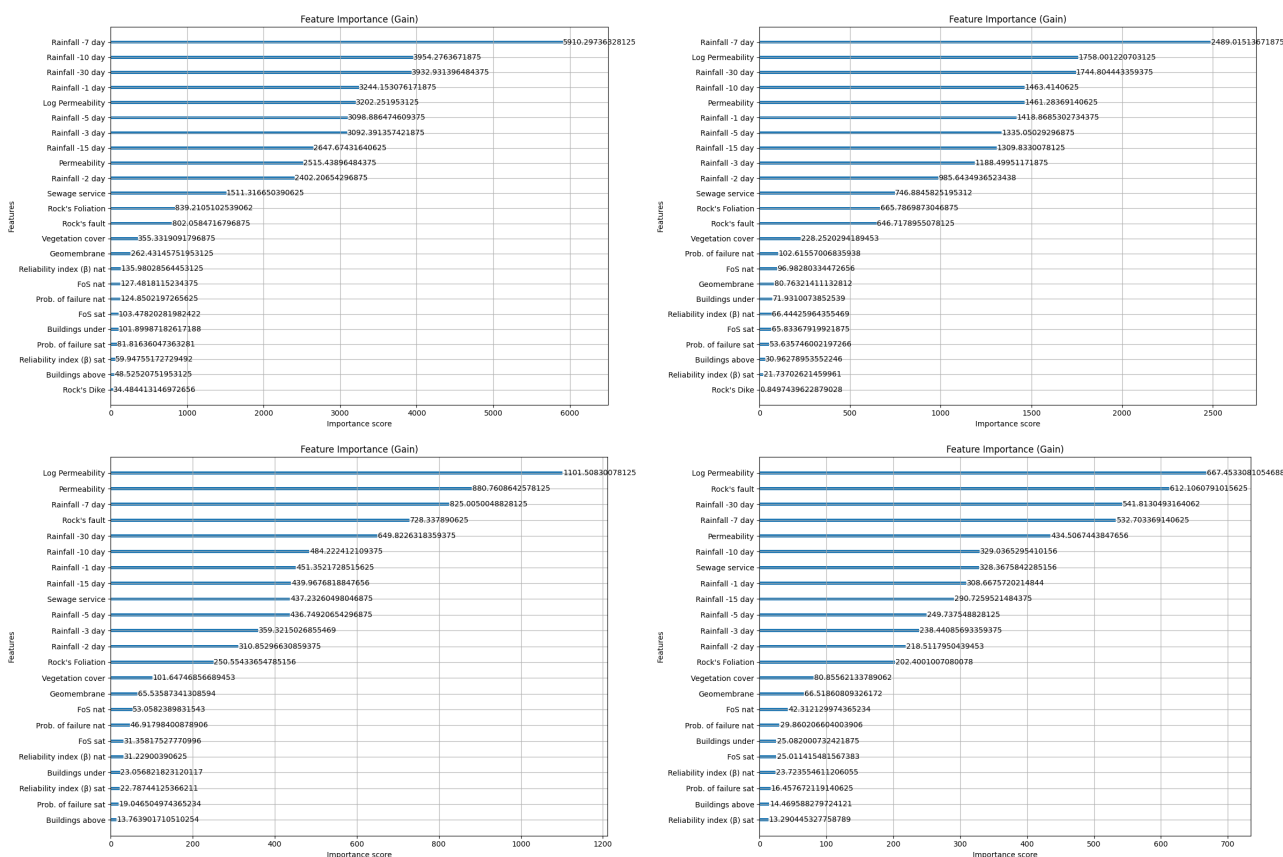


Figure 13. Importance of the features (input parameters) on the ML performance in terms gain for different  $R_i$  values



#### 4 Conclusions

255 This research paper presents a robust and effective machine learning (ML) framework for the prediction of slope instabilities in the city of Salvador, Bahia, Brazil. The primary purpose was to address the significant challenge of managing slope stability issues in urban areas with complex terrain by developing a data-driven model capable of providing accurate, real-time predictions of soil mass movements. This model was designed to serve as a critical decision-support tool for municipal authorities, enabling proactive risk management so as to ensure public safety. The study's approach involved integrating a comprehensive  
260 dataset comprising 13,522 emergency calls (about both confirmed and unconfirmed mass movements) with a digital terrain model (DTM) and extensive geotechnical data. A suite of georeferenced variables was used as input for the ML model, including cumulative rainfall over various time intervals, vegetation cover, key geological structures such as faults and foliations, the status of the sewage collection system, and residential density, both at the slopes's foot and crest. The XGBoost algorithm, a powerful gradient boosting technique, was used to build the predictive model, which was rigorously trained and validated. The  
265 results of this study are highly compelling and demonstrate the significant potential of ML in geotechnical hazard prediction. The model achieved an outstanding performance, with an  $R^2$  value consistently exceeding 0.94 across various scenarios and reaching a peak of approximately 0.98 during both the validation and testing phases. This exceptional accuracy underscores the model's reliability in forecasting slope instability events. A detailed analysis of feature importance revealed that variables directly related to slope stability, such as the Factor of Safety (FoS) and probability of failure, along with cumulative rainfall and the quality of the sewage service, were the most influential predictors. The model's performance was found to be sensitive  
270 to parameters like the slope's radius of influence (Ri) and the weighting of confirmed versus unconfirmed emergency calls (RFU), with an Ri of 150m and an RFU of 20 yielding physically consistent optimal results. The practical implications of this research, particularly for evacuation alarming in high-risk situations, are profound. The high predictive accuracy of the model provides a solid foundation for developing an effective early warning system. By continuously processing real-time data on  
275 rainfall and other dynamic factors, the system can identify areas where the risk of slope failure has surpassed critical thresholds. This enables municipal authorities to issue timely and targeted evacuation orders, thereby minimizing the risk to human life and property. The model's ability to be frequently updated with new emergency call data and weather information ensures its dynamic nature, allowing it to adapt to changing conditions and improve its predictive power over time. Ultimately, this work provides a scalable and efficient tool that can be integrated into existing municipal warning systems, transforming reactive re-  
280 sponses into proactive risk mitigation strategies and significantly enhancing the resilience of communities vulnerable to slope instability hazards.

*Code availability.* The software code developed for the paper can be made available upon request to the authors and as part of a cooperation agreement between institutions.



285 *Data availability.* The article's experimental data can be made available upon request to the authors. The emergency calls from the population to the city hall may contain sensitive information, and their disclosure to a third party is only possible after filtering and approval by the city administration.

*Code and data availability.* The code data generated for the paper can be made available upon request to the authors and as part of a cooperation agreement between institutions.

290 *Author contributions.* SLM and MFC are responsible for Conceptualization and methodology. JSSO and EP are responsible for data curation. SLM, GBS, JSSO, and SLM are responsible for formal analysis and validation. GBS is responsible for software development. SLM, MFC, JSSO, EP, and MK are responsible for supervision, and SLM and MK are responsible for writing.

*Competing interests.* The authors declare have no competing interests that are directly or indirectly related to the work submitted for publication.

*Acknowledgements.* The authors would like to acknowledge all the support provided by the Salvador city's municipality.



## 295 References

- Ahangari Nanekharan, Y., Pusatli, T., Chengyong, J., Chen, J., Cemiloglu, A., Azarafza, M., and Derakhshani, R.: Application of Machine Learning Techniques for the Estimation of the Safety Factor in Slope Stability Analysis, *Water*, 14, 3743, <https://doi.org/10.3390/w14223743>, 2022.
- ASTM-D7181: Standard Test Method for Consolidated Drained Triaxial Compression Test for Soils, Tech. rep., ASTM, <https://doi.org/10.1520/D7181>, 2011.
- ASTM\_D3080: Standard Test Method for Direct Shear Test of Soils Under Consolidated Drained, Tech. rep., ASTM International, <https://doi.org/10.1520/D3080>, 2012.
- Baecher, G. B.: 2021 Terzaghi Lecture: Geotechnical Systems, Uncertainty, and Risk, *J. Geotech. Geoenviron. Eng.*, 149, 03023 001, <https://doi.org/10.1061/JGGEFK.GTENG-10201>, 2023.
- 305 Barbosa, J. S. F., Correa-Gomes, L. C., Dominguez, J. M. L., Cruz, S. A. S., and Souza, J. S. D.: PETROGRAFIA E LITOGEOQUÍMICA DAS ROCHAS DA PARTE OESTE DO ALTO DE SALVADOR, BAHIA, RBG, 35, 09–22, <https://doi.org/10.25249/0375-7536.200535S40922>, 2005.
- Bishop, A. W.: The Use of the Slip Circle in the Stability Analysis of Slopes, *Géotechnique*, 5, 7–17, <https://doi.org/10.1680/geot.1955.5.1.7>, 1955.
- 310 Chen, T. and Guestrin, C.: XGBoost: A Scalable Tree Boosting System, in: Proceedings of the 22nd ACM SIGKDD International Conference on Knowledge Discovery and Data Mining, Kdd '16, pp. 785–794, ACM, New York, NY, USA, ISBN 978-1-4503-4232-2, <https://doi.org/10.1145/2939672.2939785>, 2016.
- Cherubini, C.: Reliability Evaluation of Shallow Foundation Bearing Capacity on  $c' \phi'$  Soils, *Can. Geotech. J.*, 37, 264–269, <https://doi.org/10.1139/t99-096>, 2000.
- 315 de Lima, O. A. L.: Caracterização Hidráulica e Padrões de Poluição No Aquífero Recôncavo Na Região de Camaçari - Dias D'Avila., Ph.D. thesis, Universidade Federal da Bahia, 1999.
- Dos Santos Pereira, S. A., Gitirana, G. D. F., Mendes, T. A., and Gomes, R. D. A.: Artificial Neural Networks for the Prediction of the Soil-Water Characteristic Curve: An Overview, *Soil and Tillage Research*, 248, 106 466, <https://doi.org/10.1016/j.still.2025.106466>, 2025.
- Fannin, R. J., Mickovski, S. B., Stokes, A., Eliadorani, A. A., and McConnell, R.: Debris Flow Behaviour and Travel Distance: Col Du Sabot, France, *Environmental Geotechnics*, 4, 19–26, <https://doi.org/10.1680/envgeo.14.00042>, 2015.
- 320 Fenton, G. A. and Griffiths, D. V.: Risk Assessment in Geotechnical Engineering, Wiley, 1 edn., ISBN 978-0-470-17820-1 978-0-470-28470-4, <https://doi.org/10.1002/9780470284704>, 2008.
- Ghasemian, A., Karimpour-Fard, M., and Nadi, B.: Reliability Analysis and Risk Assessment of a Landfill Slope Failure in Spatially Variable Municipal Solid Waste, *Int. J. Environ. Sci. Technol.*, 21, 5543–5556, <https://doi.org/10.1007/s13762-023-05451-1>, 2024.
- 325 Griffiths, D. V. and Fenton, G. A.: Probabilistic Slope Stability Analysis by Finite Elements, *J. Geotech. Geoenviron. Eng.*, 130, 507–518, [https://doi.org/10.1061/\(ASCE\)1090-0241\(2004\)130:5\(507\)](https://doi.org/10.1061/(ASCE)1090-0241(2004)130:5(507)), 2004.
- Griffiths, D. V., Huang, J., and Fenton, G. A.: Influence of Spatial Variability on Slope Reliability Using 2-D Random Fields, *J. Geotech. Geoenviron. Eng.*, 135, 1367–1378, [https://doi.org/10.1061/\(ASCE\)GT.1943-5606.0000099](https://doi.org/10.1061/(ASCE)GT.1943-5606.0000099), 2009.
- Javankhoshdel, S. and Bathurst, R. J.: Simplified Probabilistic Slope Stability Design Charts for Cohesive and Cohesive-Frictional ( $c - \phi$ ) Soils, *Canadian Geotechnical Journal*, 51, 1033–1045, <https://doi.org/10.1139/cgj-2013-0385>, 2014.
- 330



- Kinde, M., Getahun, E., and Jothimani, M.: Geotechnical and Slope Stability Analysis in the Landslide-Prone Area: A Case Study in Sawla – Laska Road Sector, Southern Ethiopia, *Scientific African*, 23, e02 071, <https://doi.org/10.1016/j.sciaf.2024.e02071>, 2024.
- Li, L., Jamieson, K., DeSalvo, G., Rostamizadeh, A., and Talwalkar, A.: Hyperband: A Novel Bandit-Based Approach to Hyperparameter Optimization, *Journal of Machine Learning Research*, 18, 1–52, 2018.
- 335 Lumb, P.: Safety Factors and the Probability Distribution of Soil Strength, *Can. Geotech. J.*, 7, 225–242, <https://doi.org/10.1139/t70-032>, 1970.
- Mehdzadeh, M. J., Shariatmadari, N., and Karimpour-Fard, M.: Probabilistic Slope Stability Analysis in Kahrizak Landfill: Effect of Spatial Variation of MSW's Geotechnical Properties, *Bulletin of Engineering Geology and the Environment*, <https://doi.org/10.1007/s10064-019-01688-8>, 2020.
- 340 Michalowski, R. L.: Stability Charts for Uniform Slopes, *Journal of Geotechnical and Geoenvironmental Engineering*, 128, 351–355, [https://doi.org/10.1061/\(ASCE\)1090-0241\(2002\)128:4\(351\)](https://doi.org/10.1061/(ASCE)1090-0241(2002)128:4(351)), 2002.
- Morgenstern, N. R. and Price, V. E.: The Analysis of The Stability of General Slip Surfaces, *Géotechnique*, 15, 79–93, <https://doi.org/10.1680/geot.1968.18.3.393>, 1965.
- Nascimento, S. A. d. M.: Diagnóstico Hidrogeológico, Hidroquímico e Da Qualidade Do Aquífero Freático Do Alto Cristalino de Salvador-BA, Tese de doutorado, Univeridade Federal da Bahia, Salvador-BA, 2008.
- 345 Neves, J. P., Cavalcante, A. L. B., Costa, G. D. A., and Mendes, T. A.: Landslide Prediction for Slopes Considering The Influence of Environmental and Geotechnical Factors Through Machine Learning, *RGSA*, 19, e013 161, <https://doi.org/10.24857/rgsa.v19n8-049>, 2025.
- Pedregosa, F., Varoquaux, G., Gramfort, A., Michel, V., Thirion, B., Grisel, O., Blondel, M., Prettenhofer, P., Weiss, R., Dubourg, V., Vanderplas, J., Passos, A., Cournapeau, D., Brucher, M., Perrot, M., and Duchesnay, E.: Scikit-Learn: Machine Learning in Python, *Journal of Machine Learning Research*, 12, 2825–2830, 2011.
- 350 Pereira, R. H. M. and Barbosa, R. J.: Standard Specifications for Transportation Materials and Methods of Sampling and Testing: Specifications, Brasília-DF, <https://doi.org/https://CRAN.R-project.org/package=censobr>, 2023.
- Phoon, K.-K. and Kulhawy, F. H.: Evaluation of Geotechnical Property Variability, *Can. Geotech. J.*, 36, 625–639, <https://doi.org/10.1139/t99-039>, 1999.
- 355 RocScience: Slide2: Slope Stability Verification Manual, 2025.
- Santana, J. O.: A INFLUÊNCIA DOS FATORES FÍSICOS NA OCORRÊNCIA DE DESLIZAMENTOS EM ENCOSTAS: UM ESTUDO DE CASO NO MORRO DO CALABETÃO EM SALVADOR - BA, Mestrado, Univeridade Federal da Bahia, Salvador-BA, 2021.
- Silva, F., Lambe, T. W., and Marr, W. A.: Probability and Risk of Slope Failure, *J. Geotech. Geoenviron. Eng.*, 134, 1691–1699, [https://doi.org/10.1061/\(ASCE\)1090-0241\(2008\)134:12\(1691\)](https://doi.org/10.1061/(ASCE)1090-0241(2008)134:12(1691)), 2008.
- 360 Souza, L. A. P. and Gandolfo, O. C. B.: Métodos Geofísicos Em Geotecnia e Geologia Ambiental, *Revista Brasileira de Geologia de Engenharia e Ambiental*, 2, 9–28, 2012.
- Souza-Oliveira, J. S. D., Peucat, J.-J., Barbosa, J. S. F., Correa-Gomes, L. C., Cruz, S. C. P., Leal, Â. B. M., and Paquette, J.-L.: Litho-geochemistry and Geochronology of the Subalkaline Felsic Plutonism That Marks the End of the Paleoproterozoic Orogeny in the Salvador-Esplanada Belt, São Francisco Craton (Salvador, State of Bahia, Brazil), *Braz. J. Geol.*, 44, 221–234, <https://doi.org/10.5327/Z2317-4889201400020004>, 2014.
- 365 Stead, D. and Wolter, A.: A Critical Review of Rock Slope Failure Mechanisms: The Importance of Structural Geology, *Journal of Structural Geology*, 74, 1–23, <https://doi.org/10.1016/j.jsg.2015.02.002>, 2015.



- ter Braak, C. J. F. and Šmilauer, P.: R Core Team, 2018. R: A Language and Environment for Statistical Computing, Microcomputer Power, Ithaca, 2018.
- 370 Trinidad, M. and Momayez, M.: Machine Learning in Slope Stability: A Review with Implications for Landslide Hazard Assessment, *GeoHazards*, 6, 67, <https://doi.org/10.3390/geohazards6040067>, 2025.
- Wang, Y. and Akeju, O. V.: Quantifying the Cross-Correlation between Effective Cohesion and Friction Angle of Soil from Limited Site-Specific Data, *Soils and Foundations*, 56, 1055–1070, <https://doi.org/10.1016/j.sandf.2016.11.009>, 2016.
- Wong, F. S.: First-Order, Second-Moment Methods, *Comput. Struct.*, 20, 779–791, [https://doi.org/10.1016/0045-7949\(85\)90039-2](https://doi.org/10.1016/0045-7949(85)90039-2), 1985.
- 375 Yadav, D. K., Chattopadhyay, S., Tripathy, D. P., Mishra, P., and Singh, P.: Enhanced Slope Stability Prediction Using Ensemble Machine Learning Techniques, *Sci Rep*, 15, 7302, <https://doi.org/10.1038/s41598-025-90539-6>, 2025.